A rupture directivity adjustment model and its application in seismic hazard

Jeff Bayless[1] [iD]**, Norman A Abrahamson[2], and Paul G Somerville[1]**

Abstract

This article contains a rupture directivity adjustment model for strike-slip earthquakes that can be applied to a traditional ground-motion model (GMM; one without explicit treatment of rupture directivity) to incorporate rupture directivity effects in either deterministic or probabilistic seismic hazard analyses. Application of the directivity model requires adjustments to both the GMM median and aleatory variability. The model described herein supersedes the previous models for strike-slip earthquakes developed by the authors of this article (Abrahamson, 2000; Bayless et al., 2020; Somerville, 2003; and Somerville et al., 1997; chapter 2 of Spudich et al., 2013). A key feature of the directivity model is that it is centered because it does not alter the magnitude and distance scaling of the GMM when averaged over uniformly distributed sites at a given rupture distance. Additionally, we address a longstanding issue regarding the directivity condition contained in the NGA-W2 dataset (Ancheta et al., 2014) and conclude that the biases in the mean and standard deviation of directivity effects are small enough to ignore for the purposes of modeling directivity. We provide guidance on the directivity model implementation, including a review of deterministic and probabilistic seismic hazard applications, and recommend methods for modeling hypocenter locations and multisegment ruptures. The model addresses the RotD50 (Boore et al., 2010) horizontal component of 5% damped spectral acceleration. A future update will address directionality and directivity effects for other styles of faulting. Implementations of the model are provided in the electronic supplement.

Keywords

rupture directivity, ground-motion model, probabilistic seismic hazard, deterministic seismic hazard

Date received: 27 February 2024; accepted: 18 September 2024

[1]AECOM, Los Angeles, CA
[2]UC Berkeley, Berkeley, CA

Corresponding author:
Jeff Bayless, AECOM, 300 S. Grand, Los Angeles, CA 90071.
Email: jeff.bayless@aecom.com

Introduction

The spatial variations in near-source ground-motion amplitude and duration due to the effects of rupture propagation, source radiation pattern, and the polarization of seismic waves have been categorized jointly as "rupture directivity" effects in the engineering-seismology literature (Spudich et al., 2013). Forward directivity occurs when the rupture front propagates toward the site at a velocity close to the shear wave velocity, and the rupture direction is consistent with the direction of slip on the fault (Somerville et al., 1997). Forward directivity conditions are generally characterized by coherent pulses of the seismic energy, leading to larger-than-average, long-period, ground-motion amplitudes over a shortened duration relative to ordinary ground motions. Backward directivity occurs when the rupture propagates away from the site and generally gives rise to smaller-than-average, long-period, ground-motion amplitudes over longer durations (Somerville, 2003).

The effects of rupture directivity on near-fault ground motions are known to be significant and should be included to accurately estimate the hazard, especially for long-period ground motions (Abrahamson, 2000). However, rupture directivity effects are not explicitly accounted for in typical ground-motion models (GMMs) and, therefore, not in typical probabilistic seismic hazard analyses (PSHAs). The primary obstacle for implementation in practice is because substantial confusion exists in practice about which directivity models (DMs) to use and how to apply them to the median and aleatory variability of GMMs, especially to complex multisegment rupture models (Donahue et al., 2019). For example, the 2023 United States National Seismic Hazard Model considered implementing DMs but decided to delay their use until there is more agreement in the modeling community concerning how to represent rupture directivity effects (Petersen et al., 2024). Overviews of existing directivity models are given in Al Atik et al. (2023) and Donahue et al. (2019).

In this article, we update our rupture directivity model previously developed under USGS Award G18AP00092 (Bayless et al., 2020; Bea20). The directivity model described herein is referred to as Bea24. This update applies to strike-slip earthquakes and includes formalized instructions for adjustments to the median and aleatory variability of the GMM to which the model is applied. In the response spectral approach, which we adopt, rupture directivity effects are considered by applying adjustment factors (for the median and standard deviation) to the models for the elastic acceleration response spectrum at 5% damping. Bea24 addresses the RotD50 (Boore et al., 2010) horizontal component of spectral acceleration, which is the median (50th percentile) of the geometric means computed from the as-recorded orthogonal horizontal motions rotated through all possible nonredundant rotation angles and is modeled in the NGA-W2 GMMs (summarized in Gregor et al., 2014). The response spectral approach lends itself readily to inclusion into PSHA (Rodriguez-Marek and Cofer, 2009).

The Bea24 model is suitable for use in future PSHAs, including those performed as part of the US National Seismic Hazard Model. Future updates will address directivity effects for other styles of faulting and may address directionality by providing models for the fault-normal and fault-parallel orientations (e.g. Somerville et al., 1997). Bea24 supersedes the previous models developed by the authors of this article: Bea20 (Bayless et al., 2020), BS13 (chapter 2 of Spudich et al., 2013), Somerville (2003), Abrahamson (2000), and Somerville et al. (1997). Supplemental Appendix A provides model implementations in MATLAB and FORTRAN languages: the model is implemented in the open-source hazard software HAZ45.2 (Abrahamson, 2024; Hale et al., 2018).

The remainder of this article contains the following topics. First, we clarify directivity modeling concepts that have been longstanding sources of confusion in practice. Then, the Bea24 rupture directivity adjustment model is presented. Procedures for the deterministic and probabilistic applications of the rupture directivity model are given, along with examples, followed by our conclusions.

Directivity centering

When modeling rupture directivity effects, the issue of "centering" has been a longstanding source of confusion in practice. This is because the term has been used in reference to two different concepts:

1. The directivity condition of the mean and standard deviation (of directivity effects) in an existing GMM or GM dataset. To distinguish from the second concept, this is referred to as "**neutrality**" of the directivity condition hereafter. Neutrality is a sampling bias issue and is related to a dataset or a GMM derived from a dataset.
2. The directivity condition of a DM used with a traditional GMM (one that does not explicitly include a term for rupture directivity effects). A "**centered**" DM does not alter the magnitude and distance scaling of the GMM when averaged over uniformly distributed sites at a given rupture distance. Centering is related to a directivity model.

For a directivity adjustment model to be used in seismic hazard analyses to modify a GMM, it is critical that the directivity model is **centered** and to confirm that the directivity condition of the mean and standard deviation of the dataset used to derive the directivity model is sufficiently **neutral.** The centering is required so that the directivity adjustment model does not alter the magnitude or distance scaling of the GMM. The check for neutrality is required to confirm that the average directivity condition contained within the empirical data (and any model derived from it) is not biased. These concepts are discussed further in Supplemental Appendix B.

Supplemental Appendix B also contains a detailed evaluation of the neutrality of the mean and standard deviation of the directivity condition of the NGA-W2 database and GMMs. We conclude that the mean directivity condition of the database has a small bias toward forward directivity. That bias varies with distance and spectral period; at its largest, it is approximately 5% at long spectral periods and close distances. The forward-directivity bias is smaller at shorter spectral periods and larger distances. To the extent that Bea24 is based on the NGA-W2 recordings, we have assumed that the bias in the mean directivity condition, over all distances and spectral periods, is small enough to ignore. This conclusion is consistent with Donahue et al. (2019).

The standard deviations of the directivity effect at the NGA-W2 recording stations are not inconsistent with the standard deviations of the directivity effect at all possible station locations. Therefore, to the extent that the standard deviation of the NGA-W2 GMM models contains rupture directivity effects, these models can be considered to reflect a directivity-neutral condition of the standard deviation of directivity effects.

Rupture directivity adjustment model

This section describes the centered rupture directivity adjustment model, Bea24, including components for the median and aleatory variability. The model is rooted in two basic Somerville et al. (1997) insights—namely that (1) forward directivity occurs when the rupture front propagates toward the site (at a velocity close to the shear wave velocity) and the direction of slip on the fault is aligned with the site, and (2) the directivity effect is stronger when the distance the rupture travels is longer. Together, these two insights imply that the directivity amplification will be largest in areas where simultaneously the horizontally propagating shear wave radiation pattern lobe (for a point-source double couple at the hypocenter) is peaked and in areas where the rupture has propagated in that direction for some distance.

The complete model development process is outlined in Supplemental Appendices D and E. The remainder of this section describes the Bea24 model, the required input parameters, constraints, and limitations, and identifies the significant changes from Bea20.

Coordinate system

The model relies on the generalized coordinate system GC2, as formulated by Spudich and Chiou (2015). GC2 defines the strike-normal (T) and strike-parallel (U) coordinates (in km) of sites located around complex fault geometries, including those that are neither straight nor continuous. Spudich and Chiou (2015) prefer placing the GC2 origin at the first endpoint of the fault trace so that U along the rupture trace is positive. For our application, we define the origin to be the rupture surface trace ordinate of the up-dip projection of the hypocenter. This is convenient for converting U into our directivity prediction parameter S, which is the rupture travel length measured along the strike relative to the hypocenter (described below). With this choice of origin, S is positive in the direction of strike and negative in the anti-strike direction. A MATLAB function for calculating GC2 is provided in Appendix A, and GC2 is implemented in the open-source PSHA software HAZ45 (Abrahamson, 2024; Hale et al, 2018).

Note that the fault parallel ordinate, T (km), should not be confused with the spectral acceleration oscillator period, also denoted T (sec). In this article, we italicize the GC2 ordinate T and provide the units of the oscillator period T (e.g., T = 4 sec) whenever possible to avoid confusion.

Median directivity adjustment model

The median prediction of a nondirective GMM can be adjusted using Equation 1:

$$\ln(RotD50_{dir}(\boldsymbol{M}, \text{T}, X)) = \ln(RotD50_{GMM}(\boldsymbol{M}, \text{T}, X)) + f_D(M, \text{T}, x) \quad (1)$$

where $RotD50_{dir}$ is the GMM prediction with the directivity adjustment, $RotD50_{GMM}$ is the unmodified GMM-predicted ground-motion, f_D is the median directivity adjustment, $\boldsymbol{M}$ is moment magnitude, T is the oscillator period in seconds, X is the vector of additional GMM explanatory parameters (distance, site parameters, style of faulting, basin parameters, etc.), and x is the vector of parameters describing the position of the site relative to the rupture. The median directivity adjustment in natural log units, f_D, is given by Equation 2:

$$f_D(\boldsymbol{M}, \mathrm{T}, x) = A(\boldsymbol{M}, \mathrm{T}) \left(\frac{2}{1 + \exp[-k\, f_G'(\boldsymbol{M}, x)]} - 1 \right) \tag{2}$$

in which k is a constant, $A(\boldsymbol{M}, \mathrm{T})$ is a magnitude- and period-dependent model parameter, and $f_G'(\boldsymbol{M}, x)$ is the centered directivity predictor. Equation 2 is a form of the logistic function, which is a family of mathematical models used to describe exponential growth with limiting upper and lower bounds. In Equation 2, the limiting upper and lower bound is $\pm A$, with an inflection point at $f_G' = 0$. With this functional form, the median directivity adjustment is limited to be $f_D = +A$ when f_G' is large and positive (forward directivity) and is limited to $f_D = -A$ when f_G' is negative with a large absolute value (backward directivity). When the centered directivity predictor is equal to zero ($f_G' = 0$), the median directivity adjustment is also equal to zero ($f_D = 0$). The model parameter k represents the slope of the relationship between f_G' and f_D. The period-dependence of f_D is incorporated through $A(\boldsymbol{M}, \mathrm{T})$, which is modeled with a Gaussian function of period with magnitude-dependent peak period. Table 1 lists the median model coefficient values.

Directivity Predictor, f_G

The centered directivity predictor is calculated using Equation 3a:

$$f_G'(\boldsymbol{M}, x) = [\, f_G(x) - \overline{f_G(x)}\,]\ f_{dist}(\boldsymbol{M}, x)\, f_{Ztor}(Ztor) \tag{3a}$$

$$f_G(x) = \ln(S_2)|\cos(2\theta)| \tag{3b}$$

$$S_2 = \sqrt{9 + (S\cos(Rake))^2} \tag{3c}$$

$$\theta = \left| \tan^{-1} \frac{T}{U} \right|; \ \ if\ \ T = U = 0; \ \ \theta = 0 \tag{3d}$$

where $f_G(x)$ is the geometric directivity predictor, $\overline{f_G(x)}$ is the centering term, f_{dist} is the magnitude-dependent distance taper, and f_{Ztor} is the depth-to-top of rupture (*Ztor*) taper. In Equation 3b, the function $f_G(x)$ combines the distance the rupture has traveled toward the site (S_2, via Equation 3c, which has a minimum value of 3 km so that $\ln(S_2)$ is always greater than one), with the cosine of twice the angle made between the fault strike direction and the vector from the origin to the site (θ; Equation 3d). The functions $f_G(x)$ and $\overline{f_G(x)}$ are period-independent and only depend on the source-site geometry. For notational brevity, their dependencies on x are suppressed hereafter. Equations 3a–d are independent of the spectral period, T.

Equation 3c requires the rupture representative rake angle and the parameter S, which is readily obtained from the GC2 ordinate U. Because we choose the GC2 origin to be the rupture surface trace ordinate of the up-dip projection of the hypocenter, S is equal to U for sites within the along-strike extent of the rupture (for simple ruptures, the along-strike extent is the rupture length). For sites outside the rupture length (i.e., for sites with non-zero R_{y0}), S is equal to the U ordinate of the nearest rupture trace endpoint. Examples of this conversion are given in Bea20. Equation 3d requires only the GC2 ordinates U and T.

In Equation 3a, the directivity predictor is centered by removing the centering term at a given rupture distance, $\overline{f_G}$, defined as the mean f_G value over a suite of sites located at the same distance to an earthquake over all azimuths (sites uniformly distributed on a racetrack). There is no simple analytical solution for $\overline{f_G}$, so a numerical evaluation is performed; Supplemental Appendix B documents this procedure, and the software in

Table 1. Median model coefficients.

Coefficient	Model 1 (Simulations)	Model 2 (NGA-W2)
A_{max}	0.54	0.34
k	1.58	1.58
σ_g	0.38	0.26

Supplemental Appendix A provides example implementations. The value of $\overline{f_G}$ is specific to a scenario with given hypocenter location, rupture dimensions, and rupture distance.

The rupture distances (R_{rup}) and *Ztor* tapers are applied to the centered directivity predictor in Equation 3a. These reduce the directivity adjustment to zero at *Ztor* = 20 km and at $R_{rup} = R_{max}$, where R_{max} = 60 km for **M** 6 and R_{max} = 80 km for **M** 7 and larger, as given in Equations 3e through 3g:

$$f_{Ztor}(Ztor) = \begin{cases} 1 - Ztor/20 & \text{For } Ztor < 20 \text{ km} \\ 0 & \text{For } Ztor \geqslant 20 \text{ km} \end{cases} \tag{3e}$$

$$f_{dist}(\textbf{M}) = \begin{cases} 1 - \exp\left(\dfrac{-4R_{max}(\textbf{M})}{R_{rup}} + 4\right) & \text{For } R_{rup} \leqslant R_{max}(\textbf{M}) \\ 0 & \text{For } R_{rup} > R_{max}(\textbf{M}) \end{cases} \tag{3f}$$

$$R_{max}(\textbf{M}) = \begin{cases} 20\textbf{M} - 60 & \text{For } 6 \leqslant \textbf{M} < 7 \\ 80 & \text{For } \textbf{M} \geqslant 7 \end{cases} \tag{3g}$$

Logistic function parameters. The logistic function in Equation 2 has a constant slope parameter, k, and limiting amplitude function, $A(\textbf{M}, \text{T})$. The amplitude function $A(\textbf{M}, \text{T})$ is modeled with a Gaussian function of period (Equation 4a). This function has a maximum value A_{max} and is centered on period T_{peak} (Equation 4b). The standard deviation (width parameter) of the Gaussian function is σ_g. The function $A(\textbf{M}, \text{T})$ is narrowband (Somerville, 2003) in that the peak period of the directivity effect increases with magnitude. The magnitude dependence of the peak period is modeled with Equation 4a.

$$A(\textbf{M}, \text{T}) = A_{max} \, exp\left(\frac{(\log_{10}\frac{\text{T}}{\text{T}_{peak}(\textbf{M})})^2}{-2\sigma_g^2}\right) \tag{4a}$$

$$\text{T}_{peak}(\textbf{M}) = 10^{-2.15 + 0.404\textbf{M}} \tag{4b}$$

Model coefficients. Values for the model coefficients k, A_{max}, and σ_g are listed in Table 2. Models are developed as described in Supplemental Appendix D; Model 1 is derived from earthquake ground-motion simulations described in Bea20, and Model 2 is derived from the NGA-W2 ground-motion database. Table 3 summarizes the model functions, model parameters (values used by the functions), arguments (values used to calculate the parameters), and coefficients.

Table 2. Description of model functions, parameters, arguments, and coefficients.

	Name	Description
Functions	f_D	Median directivity adjustment (ln units).
	f_G, $\overline{f_G}$, f_G'	Period independent geometric directivity predictor (uncentered), centering term, and centered directivity predictor
	A	Period-dependent lower and upper bound of the directivity adjustment.
	f_{Ztor}	Depth to top of rupture taper function.
	f_{dist}	Distance taper function.
	ϕ_{Red}	Within-event standard deviation reduction.
Parameters	S	The horizontal length of the rupture traveled between the site and the origin (km).
	S_2	Generalized rupture travel distance parameter that accounts for S and the rupture representative rake angle (km).
	θ	The angle made between the average fault strike direction and the vector from the origin to the site (calculated in plan view).
	T_{peak}	The peak period of the directivity effect (sec).
	R_{rup}, R_{max}	Distance parameters used in the distance taper function (km).
Arguments	U, T	The GC2 strike-parallel and strike-normal coordinates relative to the origin, which is defined as the projection of the hypocenter up-dip to the ground surface (km).
	Rupture information	The basic information about the rupture: M, segment coordinates, segment lengths, segment strike angles, depth to top of rupture, representative rake angle, and primary hypocenter location.
	T	The oscillator spectral period in sec (note the spectral period T is not italicized, and care should be taken not to confuse T with the GC2 strike-normal coordinate, *T*).
Coefficients	A_{max}	The limiting lower and upper bound of the median directivity adjustment.
	k	The logistic function slope parameter.
	σ_g	The standard deviation (width parameter) of the Gaussian function used to model the narrowband formulation.
	e_l	Aleatory variability model coefficient.

Aleatory variability adjustment model

The GMM between-event and within-event residuals are well-represented as zero-mean, independent, normally distributed random variables with standard deviations τ and ϕ (Al Atik et al., 2010). The total standard deviation in natural log units, σ, is given in Equation 5:

$$\sigma = \sqrt{\tau^2 + \phi^2} \tag{5}$$

The subscript GMM is used for the published GMM between-event, within-event, or total aleatory variability (τ_{GMM}, ϕ_{GMM}, or σ_{GMM}, respectively).

At any site i, there are two components of the total within-event variability (ϕ_i) associated with adding a directivity model in PSHA. $\phi_{Reduction}$ is the reduction of the GMM variability due to improvements in the median prediction. It is the reduction in variability caused by including the directivity term in GMM regression. The second component, $\phi_{i|UH}$, is the added aleatory variability due to the unknown hypocenter (UH) location for a future earthquake. $\phi_{i|UH}$ results from the range of additional ground-motion predictions introduced by integrating over multiple hypocenter locations, each with a different

Table 3. Period dependence of e_1 for Model 1 and Model 2.

T (sec)	0.01	0.3	0.4	0.5	0.75	1	1.5	2	3	4	5	7.5	10
Model 1 (simulations) e_1	0.000	0.000	0.0003	0.011	0.038	0.072	0.107	0.143	0.172	0.189	0.195	0.206	0.200
Model 2 (NGA-W2) e_1	0.000	0.000	0.002	0.007	0.024	0.041	0.064	0.076	0.091	0.110	0.124	0.145	0.157

directivity adjustment, in the PSHA. The $\phi_{i|UH}$ is called "parametric aleatory" variability because it is due to an additional physical behavior modeled in the GMM that is not part of the source characterization used in the hazard integral (Liou and Abrahamson, 2024). The relationship between the standard deviation terms is discussed further in Model Implementation: Probabilistic.

The models provided in this section are for standard deviation reductions ($\phi_{Reduction}$) because they are directly calculated from the reduction in the square root of the variance of the within-event residuals resulting from including the median Bea24 adjustment model. To apply the aleatory variability adjustment, a difference in variances should be taken using Equation 6:

$$\phi_{i,Dir}^2 = \phi_{GMM}^2 - \phi_{Reduction}^2 + \phi_{i|UH}^2 \tag{6}$$

in which $\phi_{i,Dir}$ directivity-adjusted, within-event variability at site i, ϕ_{GMM} is the published GMM within-event aleatory variability (without considering directivity), $\phi_{Reduction}$ is the variability reduction model, and $\phi_{i|UH}$ is the added aleatory variability due to the unknown hypocenter (UH) location for a future earthquake. Depending on the application, $\phi_{i|UH}^2$ may be added explicitly or implicitly (see Model Implementation). The total standard deviation to use with the GMM is a combination of Equations 5 and 6.

The model for $\phi_{Reduction}$ is given by Equation 7. The coefficient $e_1(T)$ is listed in Table 3 and shown in Figure 1 for the simulation-based model (Model 1) and the NGA-W2 data-based model (Model 2). The standard deviation adjustment models are appropriate over the period range 0.01 to 10 seconds, in the magnitude range **M**6.0–8.0 and only apply for sites within the footprint of the directivity model (e.g., for rupture distances less than R_{max}; this is built into Equation 7).

$$\phi_{Reduction}(T, R_{rup}, \boldsymbol{M}) = \begin{cases} e_1(T) & For\ R_{rup} < R_{max}(\boldsymbol{M}) \\ 0 & For\ R_{rup} \geqslant R_{max}(\boldsymbol{M}) \end{cases} \tag{7}$$

Model requirements and ranges of applicability

Using the model requires:

1. Definition of the strike-slip earthquake rupture, which includes **M**, segment coordinates, segment lengths, segment strike angles, the depth to the top of rupture, the rupture representative rake angle, and a primary hypocenter location.
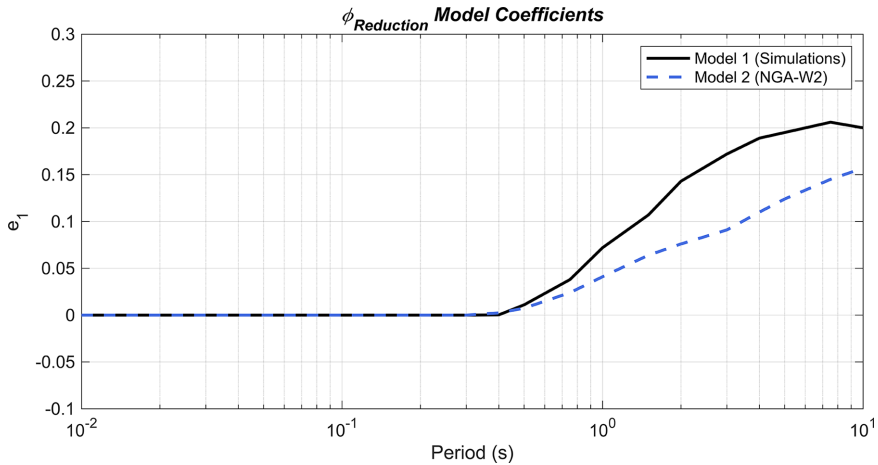
Figure 1. Within-event aleatory variability model coefficients versus spectral period.

2. The position of the site relative to the rupture, U and T, derived from the earthquake description and the site coordinates.
3. The spectral period of interest, T.

Examples of these requirements for a set of earthquake scenarios are given in Supplemental Appendix F. Supplemental Appendix A contains MATLAB and FORTRAN scripts/functions for these calculations.

Restrictions are imposed on the geometry of earthquake ruptures, as in Spudich et al. (2013). All fault *segments* are assumed to be rectangular planes with horizontal tops and bottoms and with a discrete strike angle and dip angle. One or more fault segments compose contiguous fault *strands* (which may model changes in strike and dip), and one or more fault segments compose a complete *rupture*. Multifault ruptures are defined and described in Model Implementation: Probabilistic. We follow the Aki and Richards (1980) convention where segments always dip to the right when looking along the strike direction, strike angles are measured clockwise from north, and dip angles are less than or equal to 90 degrees. Note that in this notation, *segments* relate to the discretization of a rupture model and not necessarily to any physical limits on rupture initiation and termination.

This formulation, along with the use of the GC2 coordinate system, allows the application of the model to discontinuous multisegment ruptures. In this process, the coordinate U is converted to the directivity parameter S, and the simple algorithm for S includes the distance between any disconnected ruptures. Therefore, ruptures with relatively large gaps along strike will experience artificially increased S values in some locations.

The model is designed for strike-slip earthquakes only. In forward application, we recommend categorizing an earthquake as strike-slip if it has a representative rake angle falling between one of these ranges: -180 to -150 degrees, -30 to 30 degrees, or 150 to 180 degrees. The model applies to strike-slip earthquakes in active crustal regions.

The model is appropriate over the period range 0.01 to 10 seconds for distances up to 80 km from the rupture surface trace (for larger distances, there is zero effect). The model is developed using strike-slip earthquakes in the range **M**6.0–7.9. We have tested the model

Table 4. Imposed constraints on select parameters.

Parameter	Constraint	Comment
S_2	$S_2 \leqslant 465$ km	Capped at 465 km, assumed to approximately represent the rupture length of a strike-slip **M**8.
M	$6.0 \leqslant M \leqslant 8.0$	The model was developed using the range $6.0 \leqslant M \leqslant 7.9$.

for scenario earthquakes ranging from **M**6.0 to **M**8.0 and are satisfied with the model behavior; therefore, we consider it applicable over the range **M**6.0–8.0. Table 4 lists two constraints imposed on the directivity model parameters. The limits for spectral period, magnitude, and the parameters in Table 4 are built into the MATLAB and FORTRAN functions provided in Appendix A.

The model is developed using residuals calculated from the average of three NGA-West2 GMMs: Abrahamson et al. (2014), Boore et al. (2014), and Campbell and Bozorgnia (2014). Chiou and Youngs (2014) was not included because it contains directivity adjustments. In general, we did not observe large differences between the models developed from residuals using the average of these GMMs versus the models developed from individual GMM residuals. Therefore, in forward application, it is designed to be used with these models on average or individually.

The Bea24 model described herein supersedes previous versions. Bea24 is developed for strike-slip earthquakes only and is based on two datasets: the NGA-W2 (Ancheta et al., 2014) database of recorded ground motions and the suite of strike-slip earthquake ground-motion simulations compiled in Bea20. Residual analyses were performed for both datasets independently to develop Bea24. We found that the simulations, which have significantly more near-fault stations and better azimuthal coverage than the data, demonstrate stronger scaling with the directivity parameters and over a broader period range. The NGA-W2 data generally demonstrate weaker scaling over a narrower period range. Accordingly, separate directivity model coefficients are provided for the two datasets. The models derived from both datasets have the same functional form and only differ in their coefficients.

Assumptions and limitations

Two limitations of the Bea20 model still remain. First, the simple distance and source depth tapers applied to the directivity effect are not well constrained. These tapers are ad-hoc and are imposed primarily to ensure the model is applied only within the distance ranges that are relevant in seismic hazard and for which the model was calibrated. Spudich and Chiou (2013) note that the distance taper should be a function of period because directivity can be observed at long periods at teleseismic distances, but this behavior is not modeled. Others have also observed rupture directivity effects at large distances in CyberShake simulations (Bayless and Abrahamson, 2022; Meng et al., 2023). Second, the directivity predictors used by the model are ad-hoc and intuitive in nature, and although they appear to work well, this also means that for scenarios (e.g., magnitudes, distances, periods, source-site azimuths, etc.) with little data, the model is strongly based on the assumptions about the behavior of these predictors.

The model does not account for differences between the rupture direction and the slip direction. The coefficients include the average effect of differences between the slip direction and the rupture direction. The remaining aleatory term also accounts for this

simplification in the model. In reality, the direction of rupture propagation and its consistency with the slip direction will affect the degree of rupture directivity (Aagaard et al., 2004).

Directivity effects are reasonably well-studied for strike-slip faults, and they are not well-characterized for dip-slip faults (Al Atik et al., 2023; Donahue et al., 2019; Spudich et al., 2013; Colavitti et al., 2021). Donahue et al. (2019) evaluated the similarities and differences among the five Spudich et al. (2013) directivity models for a range of rupture scenarios and found broad consistency in the directivity adjustments to the median ground-motion prediction among the five directivity models for strike-slip scenarios. For reverse scenarios, Donahue et al. (2019) found substantial differences among the five directivity models due to differences in the models' parametrization for these scenarios. These findings are consistent with Spudich et al. (2013).

From these conclusions, it is evident that capturing rupture directivity effects from thrust-faulting earthquakes is difficult. In the current study, we decided not to model directivity for reverse or normal-faulting events because of the following reasons. The first reason is related to the centering of the directivity model. Considering a hypothetical pure reverse-faulting earthquake and sites located along the rupture trace ($Rx = 0$ and $Ry0 = 0$), the Bea20 model predicts constant amplification for all azimuths. This has the effect of altering the distance scaling of reverse style of faulting earthquakes. If the centering algorithm taken for strike-slip earthquakes is applied to this scenario, $\overline{f_G} = f_G$, and the resulting directivity effect is zero. Therefore, Bea20 will require a reformulation or another centering algorithm for application to reverse and normal style-of-faulting earthquakes. The second reason is related to the neutrality. The neutrality is a sampling bias issue, and imagining a reverse faulting earthquake as a strike-slip earthquake turned on its side, the near-fault recordings stations located on the earth surface are, to some degree, aligned with the rupture plane and will have a bias toward positive (up-dip) directivity. As a result, directivity effects are captured to some degree in the constant term for reverse events (style-of-faulting GMM term).

Changes from Bea20

This model includes the following significant modifications from Bea20:

- The median directivity adjustment model is centered because its directivity predictor is centered, so there is no change to the median distance or magnitude scaling averaged over all site locations when it is applied to a GMM.
- The usable magnitude range is **M** 6–8.
- There are two alternative versions of the model; one is developed from simulations and the other is from NGA-W2 data.
- The model applies only to strike-slip style-of-faulting earthquakes.

Additionally, the model includes the following implementation changes from Bea20:

- The model uses the logistic function (Equation 2) instead of a linear relationship between the directivity predictor and the directivity effect.
- No hypocenter depth dependence.
- Addition of *Ztor* scaling.

Table 5. Deterministic implementation of the rupture directivity model for a given earthquake scenario and at a given site.

Application method	Median	Within-event aleatory variability
Hypocenter specified	$\ln(RotD50_{dir}) = \ln(RotD50_{GMM}) + f_D$	$\phi_{i,Dir}^2 = \phi_{GMM}^2 - \phi_{Reduction}^2$
Hypocenter unknown (modeled with a distribution)	$\ln(RotD50_{dir}) = \ln(RotD50_{GMM}) + \mu_{f_D}$	$\phi_{i,Dir}^2 = \phi_{GMM}^2 - \phi_{Reduction}^2 + \phi_{i\|UH}^2$

- The distance taper is a function of R_{rup} instead of the distance from the surface trace (implicitly includes *Ztor*)
- The origin for the GC2 calculation is the rupture surface trace ordinate of the up-dip projection of the hypocenter.

Model implementation: Deterministic

In a deterministic seismic hazard (DSHA) application, the directivity adjustment model can be applied to a GMM without directivity. Deterministic ground-motion percentiles such as the 84th percentile (median plus one standard deviation) should be calculated using $RotD50_{dir}$ and $\phi_{i,Dir}$.

For a given site and earthquake scenario, the simplest application is to specify a hypocenter location, calculate f_D, and adjust the GMM median using Equation 1 and the within-event aleatory variability using Equation 6; these equations are repeated in the first row of Table 5. Taking this approach, it is possible to estimate the "worst case" ground-motion scenario by selecting the hypocenter location corresponding to the largest amplification (positive f_D), or conversely, the "best case" scenario by selecting the hypocenter location corresponding to the largest de-amplification (negative f_D). With this method, the parametric variability, $\phi_{i\|UH}$, is equal to zero.

Because the hypocenter locations are not known for future earthquakes, the more appropriate method to use for DSHA is to model the hypocenter locations using a distribution. This is the approach taken in the probabilistic seismic hazard application described in Section 6. When hypocenter locations are modeled in this way, the deterministic ground motions should be calculated using the equations in the second row of Table 5, where the median ground motion is modified by μ_{f_D} and the within-event variability has a non-zero parametric variability, $\phi_{i\|UH}$.

For a given earthquake scenario and at a given site, μ_{f_D} is the weighted mean of the median directivity adjustment accounting for the uncertainty in hypocenter location:

$$\mu_{f_D}(\boldsymbol{M}, \mathrm{T}, x) = \sum_{h=1,N_h} P_h f_D(\boldsymbol{M}, \mathrm{T}, x)_h \tag{8}$$

where P_h is the probability of the h'th hypocenter location on the rupture from N_h locations approximating $f_H(h)$ such that $\Sigma_k^{N_h} P_h(h_k) = 1$, and $f_D(\boldsymbol{M}, \mathrm{T}, x)_h$ is the median directivity adjustment at site location x for hypocenter location h.

The parametric variability term $\phi_{i\|UH}$ is the added aleatory standard deviation introduced by the distribution of hypocenter locations (because each hypocenter location results

in a different value of f_D at the site). This term, which is a weighted standard deviation, should be calculated directly at each site using Equation 9:

$$\phi_{i|UH}(\boldsymbol{M}, \mathrm{T}, x) = \sqrt{\frac{\sum_{h=1}^{N_h} P_h \left(f_D(\boldsymbol{M}, \mathrm{T}, x)_h - \mu_{f_D}(\boldsymbol{M}, \mathrm{T}, x) \right)^2}{\frac{(N_h' - 1)}{N_h'} \sum_{h=1}^{N_h} P_h}} \tag{9}$$

where N_h' is the number of non-zero weights.

The choice of $f_H(h)$ has epistemic uncertainty and may be modeled as part of the logic tree of the seismic hazard model. Several models for along-strike and down-dip hypocenter distribution are available in the scientific literature (e.g., Mai et al. 2005; Melgar & Hayes, 2019; Watson-Lamprey 2018). Al Atik et al. (2023) used a uniform distribution of hypocenters along strike and down dip.

The following sections provide example applications for cases with a specified hypocenter and with an unknown hypocenter.

Scenario application with specified hypocenter

The example application of the model here uses the Landers earthquake, modeled with **M** 7.28, total length of 71.7 km, 180-degree rake, 90-degree dip, and *Ztor* = 0 (Figure 2). In this scenario, the hypocenter location is known (or specified). To use the directivity model requires the GC2 strike-normal (T) and strike-parallel (U) coordinates in km. Figure 2 shows maps of the median ground-motions and amplification factors resulting from this scenario for a 3-second spectral period. These maps use the Boore et al. (2014) GMM and assume the reference site and basin conditions in the GMM at all sites.

Figure 2a shows contours of median predicted spectral acceleration from Boore et al. (2014), which do not have azimuthal variation or any correlation with the hypocenter location. Panel b shows the contours of f_D for this scenario, hypocenter, and spectral period. Finally, panel c shows the median Boore et al. (2014) spectral acceleration amplified by the f_D values in panel b. Because the hypocenter is near the southern end of the rupture, the region to the north/northwest, including Lucerne, has significantly higher predicted ground motions after including the directivity adjustment. Conversely, in the backward directivity region (e.g., Joshua Tree), the ground motions are reduced. Figure 2d shows the within-event residuals from the Campbell and Bozorgnia (2014) GMM, which compare favorably to the directivity model for this scenario and spectral period (Figure 2b).

Figure 3 shows the median response spectra for this scenario at Lucerne and Joshua Tree, and Figure 4 shows the 84th percentile deterministic response spectra for the scenario using the directivity model median and aleatory variability adjustments (Table 5; top row).

Scenario application with unknown hypocenter

This section provides a deterministic example with unknown hypocenter location using the same Landers earthquake scenario as in the previous section. We define $N_h = 100$ equally spaced hypocenter locations along strike and use a uniform distribution to assign P_h such that $\Sigma_k^{N_h} P_h(h_k) = 1$. The directivity model is calculated for each of the 100 hypocenter locations, h_k.
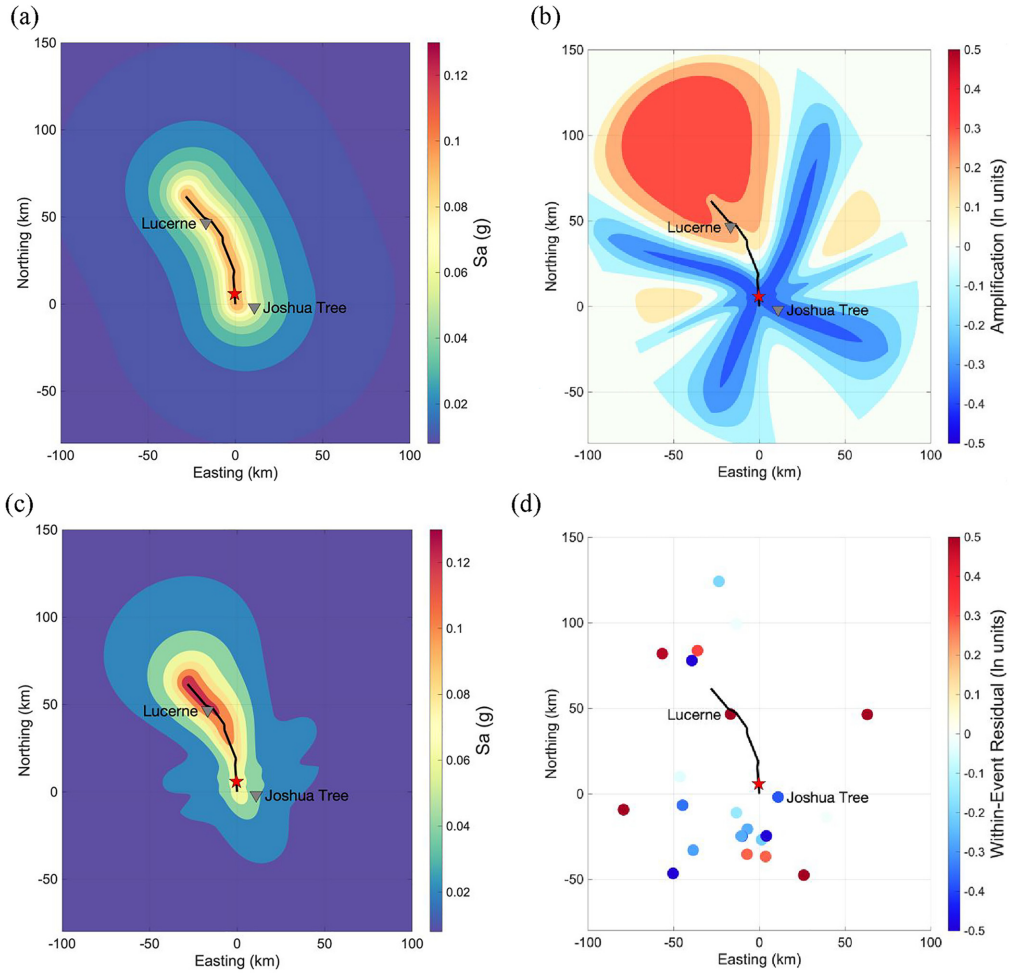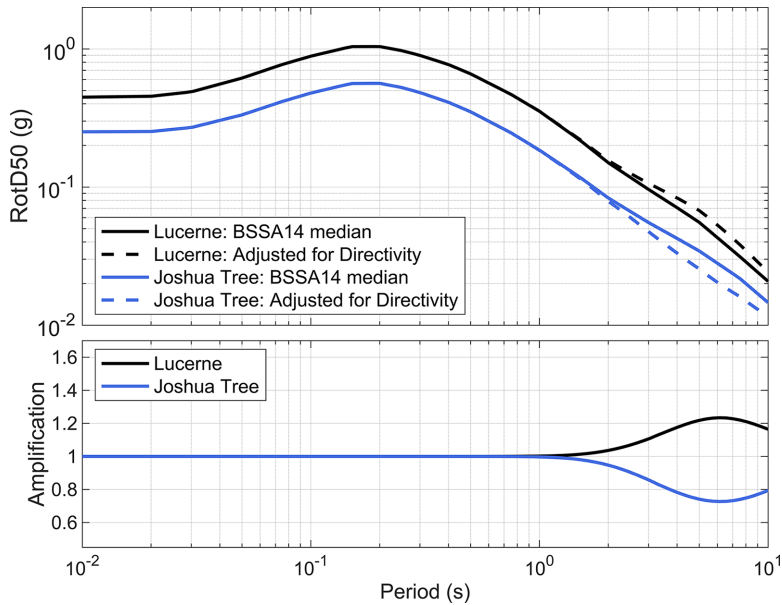
Figure 2. Deterministic application of the directivity model, Model 1 median adjustment, to the Landers earthquake with specified hypocenter at 3 seconds spectral period. In all four maps, the rupture trace is the heavy black line and the hypocenter location is the red star. (a) Contours of median predicted spectral acceleration from Boore et al. (2014). (b) Contours of f_D for this scenario and spectral period (ln units). (c) Contours of the median predicted spectral acceleration due to adjustment by the f_D values in (b). (d) Within-event residuals from Campbell and Bozorgnia (2014).

Figure 5 shows maps of μ_{f_D} and $\phi_{i|UH}$, which are calculated using Equations 8 and 9, respectively. Using this method, the deterministic ground motions at a given location are calculated using the equations in the second row of Table 5, where the median ground motion is modified by μ_{f_D} and the within-event aleatory variability has adjustments $\phi_{Reduction}$ and $\phi_{i|UH}$.

Combining Equations 5 and 6 results in Equation 10:

$$\sigma_{Dir} = \sqrt{\tau_{GMM}^2 + \phi_{GMM}^2 - \phi_{Reduction}^2 + \phi_{i|UH}^2} \qquad (10)$$
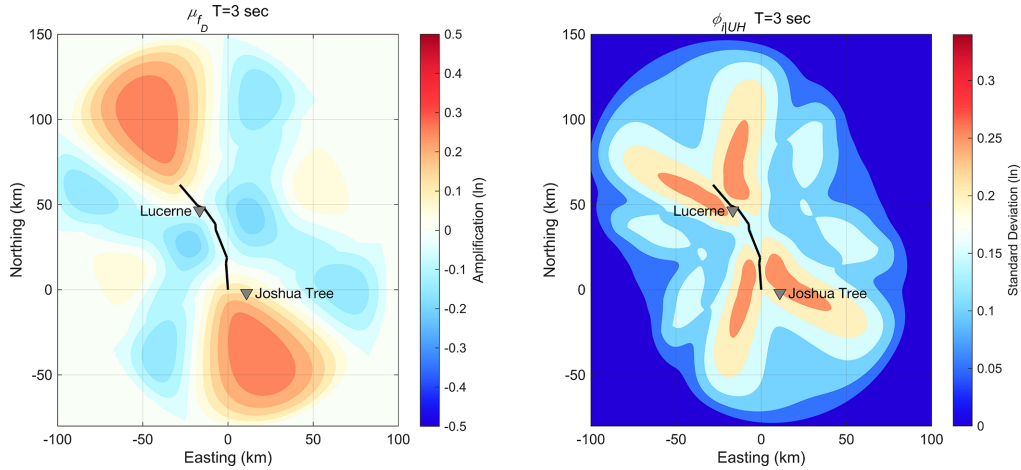
Figure 3. Deterministic application of the directivity model—Model 1 for the median adjustment—to the Landers earthquake median response spectra at Lucerne and Joshua Tree (locations shown in Figure 3).
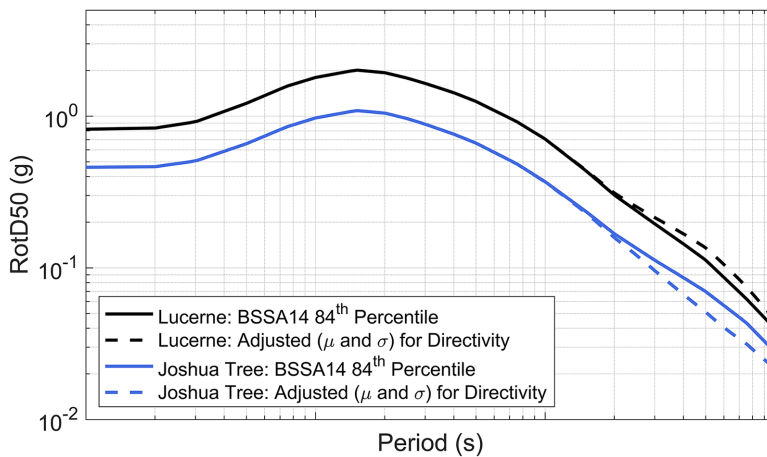
Figure 4. Deterministic application of the directivity model—Model 1 for the median and aleatory variability adjustments—to develop the Landers earthquake 84th percentile response spectra at Lucerne and Joshua Tree (locations shown in Figure 2).

In Directivity Centering, we verified that the variability of the directivity effect in the NGA-W2 data reflects a directivity-neutral (unbiased) condition. As a result, $\phi_{i|UH}$ is approximately equal to $\phi_{Reduction}$ on average. The site-specific value of $\phi_{i|UH}$ can be smaller or larger than $\phi_{Reduction}$, but they are approximately equal on average over all azimuths and distances.

Figure 5. Deterministic application of the directivity model (Model 1) to the Landers earthquake scenario with unknown hypocenter location at 3 seconds spectral period. Left: Contours of μ_{f_D} (ln units). Right: Contours of $\phi_{i|UH}$ (ln units).

In this example, and at T = 3 seconds, $\phi_{Reduction}$ = 0.172 and $\phi_{i|UH}$ ranges from 0 to about 0.25 in Figure 5. Assuming example GMM aleatory standard deviation values of τ_{GMM} = 0.35 and ϕ_{GMM} = 0.6 (σ_{GMM} = 0.69), this results in the range of σ_{Dir} = 0.67 to 0.72.

At T = 7.5 seconds, $\phi_{Reduction}$ = 0.206 and $\phi_{i|UH}$ ranges from 0 to about 0.29. Assuming example values of τ_{GMM} = 0.3 and ϕ_{GMM} = 0.6 (σ_{GMM} = 0.67), this results in the range of σ_{Dir} = 0.64 to 0.70.

Figure 6 shows maps of the T = 3 sec deterministic ground motions (median and 84th percentile) with directivity using the unknown hypocenter location method and using the Boore et al. (2014) GMM. These maps have used example GMM aleatory standard deviation values of τ_{GMM} = 0.35 and ϕ_{GMM} = 0.6 (σ_{GMM} = 0.69). The spatial pattern of predicted ground motions in Figure 6 are broadly symmetric with respect to the center of the fault trace. This is the result of modeling the future hypocenter locations using a symmetric along-strike distribution. This symmetry is in contrast with Figure 2c, which shows ground motions for the case of a specified hypocenter location and results in higher predicted ground motions to the northwest in the direction of rupture propagation.
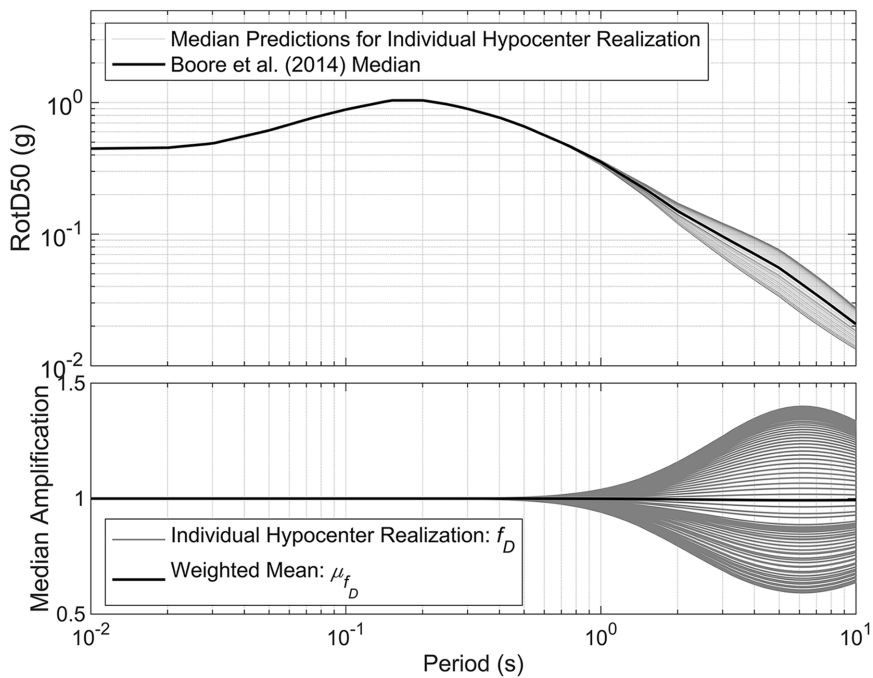
Figure 7 shows median ground motions at the Lucerne station using the unknown hypocenter location method and the Boore et al. (2014) GMM. The location of this station is shown in Figure 2. The top panel of Figure 7 shows spectral acceleration from Boore et al. (2014) along with directivity-adjusted median spectra for individual hypocenter realizations. The bottom panel shows the unweighted $\exp(f_D)$ versus spectral period for each of the 100 hypocenter realizations. Because Lucerne is located within the extent of the rupture trace, there are some hypocenters that predict forward-directivity effects (e.g., Figure 2), and there are others that predict backward-directivity effects. As a result, μ_{f_D} is approximately zero (amplification of unity) for this location using the unknown hypocenter location method.

Figure 8a compares the components of the total aleatory variability at Lucerne. For this site and scenario, $\phi_{i|UH}$ is slightly larger than $\phi_{Reduction}$ at 3 seconds spectral period,
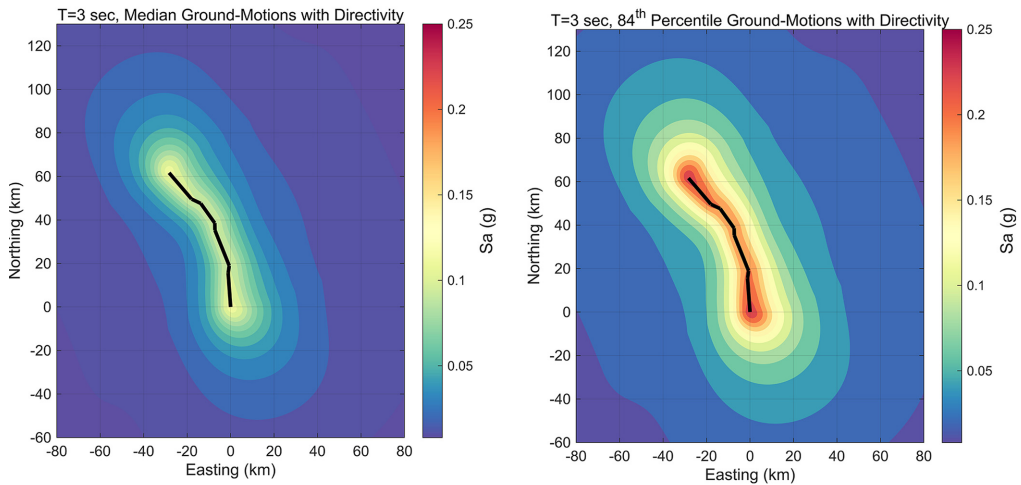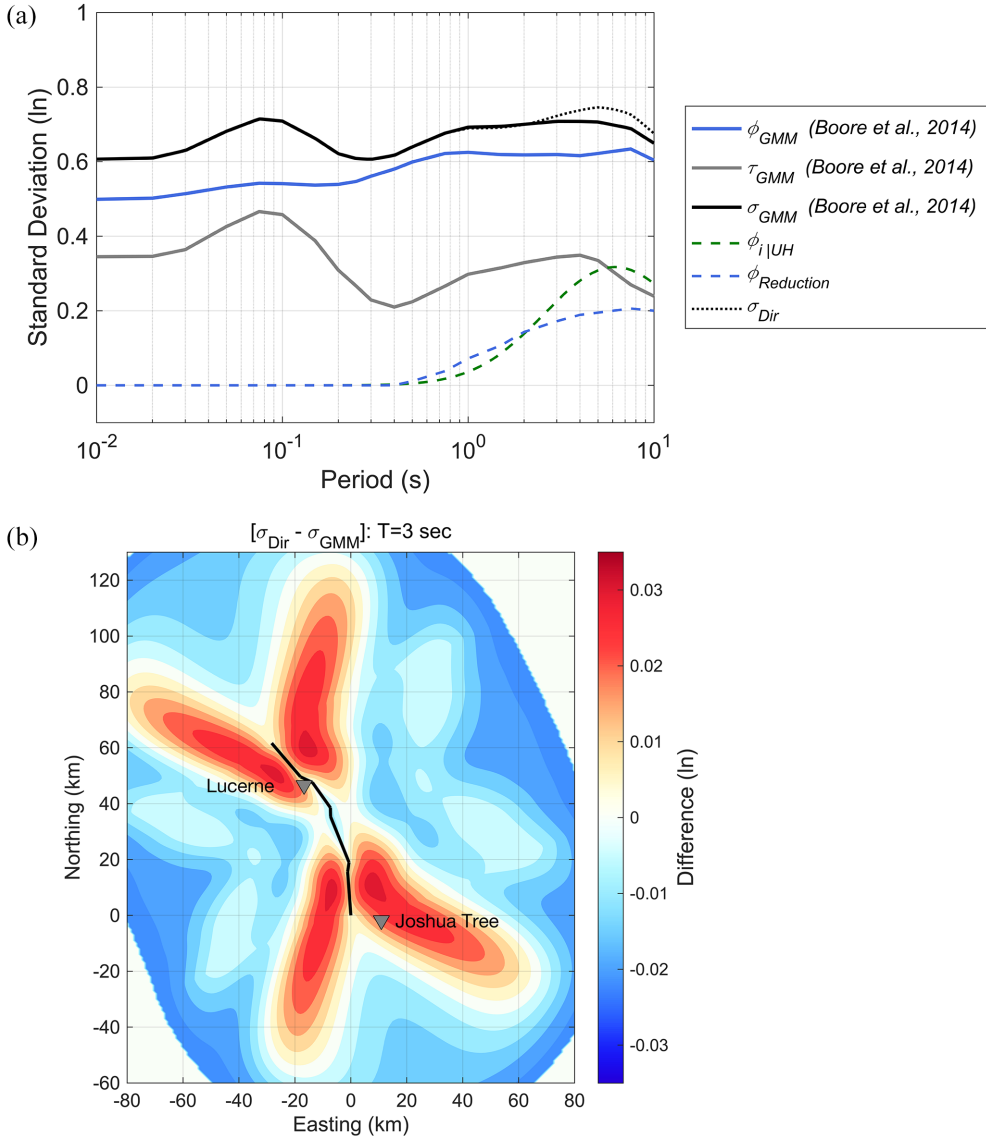
Figure 6. Deterministic application of the directivity model (Model 1) to the Landers earthquake scenario with unknown hypocenter location at 3 seconds spectral period, using the Boore et al. (2014) GMM with μ_{f_D} and $\phi_{i|UH}$ from Figure 5 and assuming $\tau_{GMM} = 0.35$ and $\phi_{GMM} = 0.6$. Left: Contours of median predicted spectral acceleration. Right: Contours of the 84th percentile predicted spectral acceleration.

Figure 7. Deterministic application of the directivity model (Model 1) to the median ground motions of the Landers earthquake scenario with unknown hypocenter location at the Lucerne station. Top: Median spectral acceleration from Boore et al. (2014) showing directivity-adjusted spectra for individual hypocenter realizations; the 100 alternative median predictions (gray) are overlapping and appear as a solid shape. Bottom: Median amplification versus spectral period for individual hypocenter realizations (exponential of f_D; unweighted) and the weighted mean (exponential of μ_{f_D}).

Figure 8. (a) Aleatory variability components versus spectral period at the Lucerne station for the deterministic application of the directivity model (Model 1) to the Landers earthquake scenario with unknown hypocenter location. (b) Contours of $\sigma_{Dir} - \sigma_{GMM}$ for the deterministic application of the directivity model (Model 1) to the Landers earthquake scenario with unknown hypocenter location.

and the net aleatory variability adjustment is small (Equation 10). Figure 8b shows a contour map of the total aleatory variability adjustment ($\sigma_{Dir} - \sigma_{GMM}$) for this scenario using the unknown hypocenter location approach. This shows how much the 84th percentile changes based on the location due to the change in total aleatory variability.

If the site-specific $\phi_{i|UH}$ is larger than $\phi_{Reduction}$, the net standard deviation adjustment is positive, implying that the variability from directivity for a given site is larger than the

range of expected directivity effects from the distribution of stations in the data set (warm colors in Figure 8b). Alternatively, a net negative adjustment implies the opposite (cool colors in Figure 8b). Neither has been documented in the literature previously, and this has been the main cause of confusion in practice about how to treat directivity effects in PSHA (Donahue et al., 2019). Directivity Centering verified that the variability of the directivity effect in the NGA-W2 data reflects a directivity-neutral (unbiased) condition. As a result, $\phi_{i|UH}$ is approximately equal to $\phi_{Reduction}$ on average. The site-specific value of $\phi_{i|UH}$ can be smaller or larger than $\phi_{Reduction}$, as shown in Figure 8b, but they are approximately equal on average overall azimuths and distances.

Including directivity effects in a DSHA with unknown hypocenters, there is a modification to the median and standard deviation as compared to the GMM without directivity. The difference in the deterministic ground motions can be an increase or decrease compared to the traditional DSHA without explicit consideration of directivity as shown by the maps in Figures 2 and 5.

Model implementation: Probabilistic

Implementation methods

In PSHA, the directivity adjustment model can be applied to a GMM without directivity using the same concepts as the deterministic application described in Model Implementation: Deterministic; for a given earthquake scenario, the GMM is modified using the directivity model median adjustment (Equation 1) and total aleatory variability adjustment (Equation 10). This requires the implementation of the directivity model into the PSHA framework, as described here.

The standard PSHA integral for point sources, without considering rupture directivity is (as modified from Baker et al., 2021):

$$\lambda(IM>z) = \sum_{i=1}^{n_{src}} N_i(\boldsymbol{M}_{min}) \int_M \int_R P(IM>z|m,r) f_M(m) f_R(r) \ dr \ dm \qquad (11)$$

where $\lambda(IM>z)$ is the annual rate of exceedance of ground motions with intensity measure (IM) greater than level z, n_{src} is the number of earthquake sources considered, $N_i(\boldsymbol{M}_{min})$ is the annual rate of earthquakes with magnitude greater than or equal to $\boldsymbol{M}_{min}$ occurring on source i, $P(IM>z|m,r)$ is the conditional probability of observing an IM greater than z for a given earthquake magnitude (m) and distance (r), and $f_M(m)$ and $f_R(r)$ are probability density functions for the magnitude and distance. $P(IM>z|m,r)$ comes from the GMM and contains an implicit integration over the GMM variability, which is typically modeled by a lognormal distribution.

For planar sources, Equation 11 also needs to consider the finite dimension and location of the rupture within the fault, so four aleatory variables (rupture width, rupture length, along strike location, and down-dip location) and their probability density functions replace the single aleatory variable r and $f_R(r)$ (Abrahamson, 2000). These are omitted here for brevity.

Hypocenter locations are not considered in conventional PSHA (Equation 11) because the traditional GMMs do not utilize the hypocenter location. When rupture directivity effects are modeled, the hypocenter locations need to be introduced. Because the hypocenter locations are not known for future earthquakes, the hypocenter locations need to be

modeled using a distribution. If the source characterization includes models for the locations of hypocenters for future earthquakes, Equation 11 can be extended to incorporate rupture directivity effects directly with Equation 12:

$$\lambda(IM{>}z) = \sum_{i=1}^{n_{src}} N_i(\boldsymbol{M}_{min}) \int_M \int_R \int_H P(IM{>}z|m,r,\theta_D) f_M(m) f_R(r) f_H(\theta_D) \; dr \; dm \; d\theta_D \tag{12}$$

where $P(IM{>}x|m,r,\theta_D)$ contains an additional vector of directivity model parameters, θ_D, and there is additional integration over the probability density function for hypocenter location on the rupture plane $f_H(\theta_D)$. $P(IM{>}z|m,r,\theta_D)$ contains both the median and standard deviation directivity adjustments and implicit integration over the GMM variability. We refer to this implementation of the rupture directivity model in the PSHA integral as the *full hypocenter randomization approach*, following the terminology of Donahue et al. (2019) and Weatherill and Lilienkamp (2023).

Sampling the hypocenter locations from a distribution adds substantial computational costs to the hazard calculation because the hypocenters need to be modeled for every relevant fault, as well as for every relevant rupture (scenario earthquake) hosted on that fault, and directivity parameters need to be calculated for each hypocenter.

Al Atik et al. (2023) applied directivity effects to their PSHA for the state of California using UCERF3 (Field et al., 2013). To implement the full hypocenter randomization approach for each site, they performed a pre-processing step outside of the hazard integral, in which the site-specific directivity parameters were calculated for every UCERF3 rupture and for uniformly distributed hypocenters. The results of this step were saved and used as look-up tables within the main hazard code, which integrates over hypocenter location and accesses the look-up table for each hypocenter. The GMM aleatory variability reduction models for each directivity model were utilized. As a result, at a given site, the mean and variability of the directivity model amplification is captured in the Al Atik et al. (2023) PSHA.

An alternative approach for explicitly modeling directivity in the PSHA integral, as presented by Watson-Lamprey (2018), is called the *modified moments* approach. This approach is to modify the moments of the GMM, for a given rupture based on the probability density function $f_H(\theta_D)$, to reflect the mean changes in the median and aleatory variability due to directivity. This allows for separation of the integration over $f_H(\theta_D)$ from the main PSHA integral and uses the mean and variance of the directivity model amplification to modify the GMM directly (Weatherill and Lilienkamp, 2023). Because of this separation, this approach is appealing for regional scale PSHAs, where the increased computation time required by the full hypocenter randomization approach may be prohibitive (Weatherill and Lilienkamp, 2023). Outside of the hazard integral, the moment modifiers (mean and variance of the directivity model amplification) can be saved using look-up tables or parametric equations.

Several techniques have been employed to determine the moment modifiers outside of the hazard integral: Watson-Lamprey (2018) fit simple parametric equations to directivity amplifications resulting from a synthetic earthquake database, Kelly et al. (2022) fit directivity amplifications from a more robust synthetic earthquake database using machine learning techniques, and Weatherill and Lilienkamp (2023) overfit an artificial neural network to the Bea20 model directivity amplification for each unique rupture in their earthquake rupture forecast. For the latter, the complete set of earthquakes in the forecast

Table 6. Approaches for implementation of the rupture directivity model in PSHA.

Approach	Median	Within-event aleatory variability
Full hypocenter randomization	$\ln(RotD50_{dir}) = \ln(RotD50_{GMM}) + f_D$ f_D is calculated for each hypocenter location of a given rupture.	$\phi^2_{i,Dir} = \phi^2_{GMM} - \phi^2_{Reduction}$ $\phi_{i\|UH}$ is implicit in integration over $f_H(\theta_D)$.
Modified moments*	$\ln(RotD50_{dir}) = \ln(RotD50_{GMM}) + \mu_{f_D}$ No modeling of hypocenter location; μ_{f_D} has been determined through integration over $f_H(\theta_D)$ outside the hazard integral.	$\phi^2_{i,Dir} = \phi^2_{GMM} - \phi^2_{Reduction} + \phi^2_{i\|UH}$ $\phi_{i\|UH}$ is added explicitly.

*The standard deviation from the modified moments approach has also been called the parametric aleatory term for the GMM (Abrahamson et al., 1990).

must be known a priori. Withers et al. (2024) implemented the Watson-Lamprey (2018) model into the USGS hazard software and tested the impact of including the model on the NSHM results.

The modified moments approach, and related machine learning techniques, are evolving topics and have significant potential for computational efficiencies in regional-scale PSHAs. For site-specific studies, the full hypocenter randomization approach may be more appropriate.

Table 6 summarizes the implementation of the directivity model into the PSHA framework for these two approaches. When the full hypocenter randomization approach is taken, f_D and $\phi_{Reduction}$ are calculated at a site for every hypocenter location of a given rupture; these are part of the term $P(IM>z|m, r, \theta_D)$ from Equation 12. The variability component $\phi_{i\|UH}$ is implicit in the integration over $f_H(\theta_D)$. When the modified moments approach is taken, there is no integration over hypocenter location, and μ_{f_D} and $\phi_{Reduction}$ are calculated at a site for a given rupture. In the modified moments approach, $\phi_{i\|UH}$ needs to be added explicitly.

The implementation of Bea24 into HAZ45.2 (Hale et al., 2018; Abrahamson, 2024) is provided in Supplemental Appendix A. The HAZ45.2 implementation uses the full hypocenter randomization approach.

Treatment of multi-fault ruptures

The UCERF3 earthquake source model is widely used in the state of California, including for the USGS National Seismic Hazard Maps. UCERF3 includes scenarios that can be categorized as "multi-fault" ruptures; those with large gaps between segments, significant changes in rupture geometry, changes in the style of faulting along strike, or a combination of these. In order to apply Bea24 to the UCERF3 and other earthquake forecasts with multi-fault ruptures, a set of rules are required.

Al Atik et al. (2023) was the first attempt to implement current generation directivity models with complex UCERF3 fault ruptures in a statewide framework. Al Atik et al. (2023) defined a multi-fault rupture (having distinct sub-faults) as a rupture that occurs on two or more non-contiguous surfaces with each surface having its own hypocenter, which are distinguished by large changes in dip and rake. A rupture was classified as multi-fault if the change in dip angle between two consecutive subsections exceeds 50 degrees, if the

change in the first quadrant rake angle between the same consecutive subsections exceeds 30 degrees, and if the gap between consecutive segments exceeds 10 km. Ruptures that did not meet the multi-fault rupture criteria were classified as "multi-segment" ruptures.

Weatherill and Lilienkamp (2023) modified the approach developed by Al Atik et al. (2023) for incorporating multi-fault ruptures into the PSHA. In summary, the ruptures classified as multi-segment are treated in the conventional manner as described in this article (a single hypocenter location distribution on the rupture plane), and the multi-fault ruptures are split up and each sub-fault rupture is characterized individually for rupture directivity effects, including distinct hypocenter location distributions for each. The maximum directivity parameter from each sub-fault is taken to represent the directivity at a given site and for a given multi-fault rupture.

Additional research is needed to evaluate the presence of rupture discontinuities and their impact on rupture directivity as well as the impact of varied multi-fault segment geometries (changes in dip angle, rake angles, and strike direction between sub-faults) on directivity effects (Al Atik et al., 2023). At this time, we recommend the Weatherill and Lilienkamp (2023) approach for categorizing and modeling multi-fault ruptures.
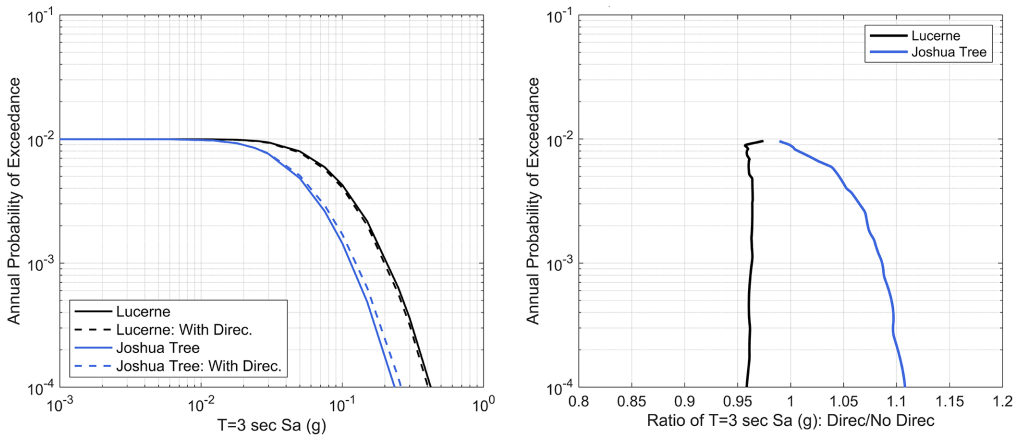
Example PSHA

This section provides an example application of Bea24 in a simple PSHA using the open-source hazard software HAZ45.2 (Abrahamson, 2024; Hale et al., 2018) with the full hypocenter randomization approach. In this PSHA, the Landers earthquake scenario from previous sections is the only source. This source is modeled as a vertical strike-slip fault with a 100-year average recurrence interval and with the pure characteristic recurrence model (**M**7.28). The Abrahamson et al. (2014) GMM is used with the reference site and basin conditions. 100 hypocenters spaced evenly along strike are used with a uniform distribution. Bea24 does not have hypocenter depth dependence, so the hypocenters down dip do not need to be modeled. The Bea24 simulation-based model (Model 1) is used including the median and aleatory variability adjustments as in Table 6.

The PSHA is performed for two sites: Joshua Tree (R_{rup} = 11.0 km) and Lucerne (R_{rup} = 2.2 km). The sites are located as shown in Figure 2. Figure 9 shows the mean hazard curves for T = 3 sec at the Joshua Tree and Lucerne sites. The dashed hazard curves have implemented the Bea24 directivity model and solid lines have no treatment of directivity. In this example, the mean hazard without directivity at Lucerne is higher than at Joshua Tree only due to their respective distances from the fault.

The right panel of Figure 9 shows ratios of the hazard curve ground-motions versus probability of exceedance, where the ratio is the hazard curve with directivity divided by the hazard curve without directivity. At the Lucerne station, which is located within the extent of the rupture trace, the inclusion of directivity reduces the T = 3 sec PSHA ground motions by a few percent. This is analogous to the deterministic application described in Model Implementation: Deterministic; at this site, there are some hypocenters that predict strong forward-directivity effects, and there are others that predict backward-directivity effects. As a result, the mean adjustment to the median considering the full distribution of future hypocenter locations is a very small reduction. The total change in aleatory variability at this site is also small; less than 0.02 ln unit increase for T = 3 sec (Figure 8).

At the Joshua Tree station, which is located off the end of the rupture trace and to the southeast, the inclusion of directivity increases the T = 3 sec PSHA ground motions by

Figure 9. Left: T = 3 sec mean hazard curves at Lucerne and Joshua Tree stations from the example PSHA, with and without rupture directivity. Right: Ratios of the T = 3 sec ground motions with and without directivity.
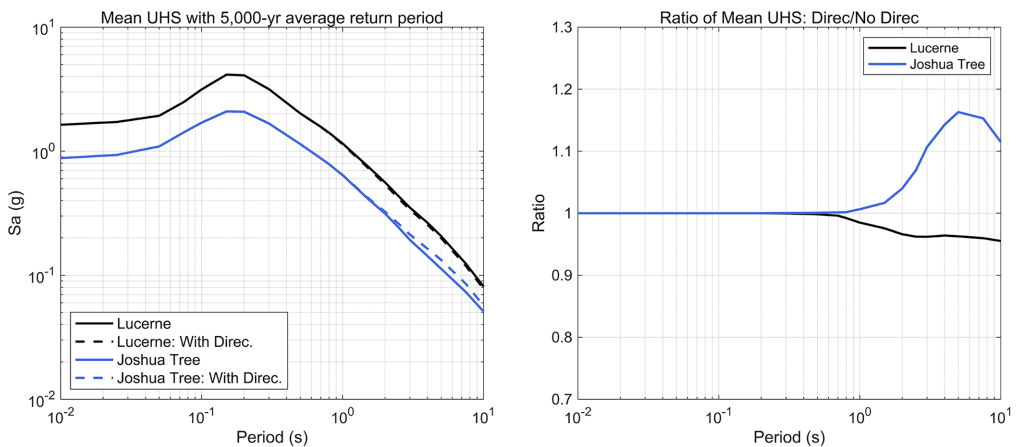
Figure 10. Left: Mean UHS with 5,000-year average return period at Lucerne and Joshua Tree stations from the example PSHA, with and without rupture directivity. Right: Ratios of the T = 3 sec ground motions with and without directivity. For each site the with and without directivity lines are overlapping for short spectral periods.

about 10 percent at longer than 1,000 year average return periods. This is again analogous to the deterministic application described previously; at this site, there are a range of median directivity adjustments from the range of potential hypocenter locations, and the mean of these increases the median ground motions. The total aleatory variability adjustment at this site is also small; less than 0.02 ln unit increase for T = 3 sec (Figure 8).

Mean uniform hazard spectra (UHS) with 5,000-year average return period are shown in Figure 10 for both sites. The right panel contains ratios of the UHS; these illustrate the period dependence of the directivity effect on the hazard for each site at this return period.
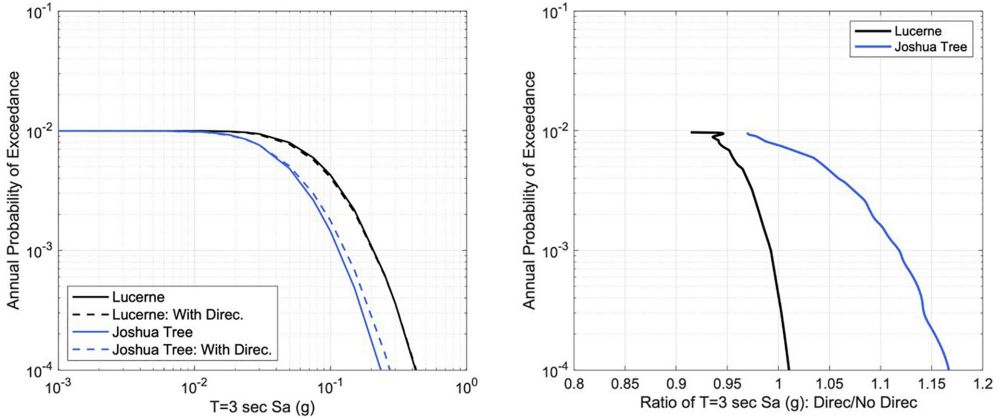
Figure 11. As in Figure 9, without applying $\phi_{Reduction}$.

Figure 11 shows mean T = 3 sec hazard curves using the full hypocenter randomization approach but without applying the reduction in aleatory variability ($\phi_{Reduction}$), which is *improper use* of the model and is shown for illustrative purposes only. Without reducing the within-event aleatory variability by $\phi_{Reduction}$, and with the implicit increase in variability from integration over the hypocenter probability density function ($\phi_{i|UH}$), the net result is an increase in total aleatory variability relative to the published GMM variability. This has the effect of artificially decreasing the slope (flattening) the mean hazard curve. To implement the directivity model into the PSHA framework correctly, the GMM aleatory variability should be appropriately reduced as outlined in this article.

Conclusions

The aim of this article is to provide an updated rupture directivity model and instructions for how to use it in seismic hazard analyses.

As part of these instructions, we clarify the term "centering" by making a distinction between concepts related to databases (the neutrality of the directivity condition) and to directivity adjustment models (centered with respect to the magnitude and distance scaling). We find that the mean directivity condition of the NGA-W2 recordings, and GMMs derived from them, have a small bias toward forward directivity. That bias is on the order of approximately 5% at long spectral periods and close distances and is smaller at short spectral periods. We have assumed that the bias in the mean directivity condition, over all distances and spectral periods, is small enough to ignore. The NGA-W2 models can be considered to reflect a directivity-neutral condition of the standard deviation. The Bea24 model is centered for all magnitudes and distances; therefore, applying it to a GMM without directivity does not alter the average magnitude and distance scaling of the GMM.

In this article, we also emphasize that application of the directivity model requires adjustments to both the GMM median and aleatory variability. The variability adjustment has a reduction component, $\phi_{Reduction}$, due to improvements in the median prediction, and an added component, $\phi_{i|UH}$, due to the unknown hypocenter location for a future earthquake. The aleatory variability adjustment depends on the PSHA implementation approach taken. If hypocenter locations are modeled explicitly in the hazard calculation

using a probability density function, the effect of the $\phi_{i|UH}$ term is implicitly included. If the mean directivity adjustment has been determined outside the hazard integral, $\phi_{i|UH}$ needs to be added explicitly to the GMM standard deviation. The standard deviation reduction component due to the improved fit, $\phi_{Reduction}$, needs to be incorporated with both approaches.

There may be an expectation by some that the directivity model should introduce larger changes to the long-period probabilistic hazard than we have shown within this article. The justification behind this perspective is that very large rupture directivity effects have been observed in recorded ground motions (e.g., the 1989 Loma Prieta; 1992 Landers, California; 1999 Kocaeli, Turkey; 1995 Kobe; and 2023 Kahramanmaraş, Turkey, earthquakes, especially on the fault-normal component at close distances to the ruptures). These observations are absolutely correct. The reason that changes to the PSHA are smaller than these observations is because the hypocenter locations are not known for future earthquakes, and so we model them using a distribution that is symmetric along strike. For a given site and rupture, there are some hypocenter locations that correspond to ground-motion amplification and there are other hypocenter locations which correspond to de-amplification. The net effect is a smaller change due to directivity than seen for a given hypocenter location. Weatherill and Lilienkamp (2023) note that a change in the probability distribution of hypocenter position toward an asymmetric one, perhaps based on a fault-specific preference for a particular direction of rupture (Ben-Zion and Sammis, 2003) would produce a significantly different pattern of amplification around the fault in a PSHA context.

For a specific DSHA scenario (fixed hypocenter), the inclusion of directivity using Bea24 can lead to significant (e.g., up to $\pm70\%$ using Model 1) changes in the long-period ground motion for specific sites depending on their location with respect to the finite fault rupture. But if the hypocenter locations are randomized for the same DSHA scenario earthquake using a symmetric distribution, the average effect of modeling directivity leads to a smaller change (e.g., up to about $\pm30\%$ for the same location).

In a PSHA, future earthquakes on all known faults are considered. Each fault hosts earthquakes with a range of possible magnitudes, and further, for each magnitude the location of the finite rupture plane within the fault is modeled (the along-strike and down-dip location). This leads to significantly more rupture scenarios in a PSHA than in a DSHA (with hypocenters modeled) for a given fault. At a site, these additional PSHA scenarios for a given fault will have varying levels of influence from the rupture directivity model because of their magnitudes, dimensions, and source-site geometries. If some of the PSHA scenarios contributing to the total mean hazard do not have strong (or any) directivity effects modeled, then the net impact of directivity on the hazard at a site will be less than for a DSHA using the same fault. As a result, a DSHA can lead to larger directivity effects than PSHA for a given fault.

As shown throughout this article and by others (e.g. Withers et al., 2023), the strike-slip directivity model adjustments are most significant off the ends of the rupture. In our example PSHA, there was only one earthquake source, for simplicity and for comparison with the DSHA example, and the "off-the-end" behavior is apparent (Figures 5 and 6). In a real PSHA for places like California, there will be many more faults modeled including a continuation of most strike-slip faults, and the "off-the-end" behavior will be reduced due to this continuation; the way the earthquake rupture forecast is segmented will impact the influence of the directivity model. Further, the superposition of directivity effects from

multiple fault sources in realistic PSHAs will complicate the effects of directivity, and depending on the setting, these effects may deconstructively interfere (Withers et al., 2023). Because of these factors, the directivity model will be more impactful for evaluations of past events and for generations of ground-motions for specific scenarios than for PSHA studies at return periods of 1,000–10,000 years.

Capturing rupture directivity effects from thrust-faulting earthquakes is difficult, and the available models for them vary greatly in terms of predicted amplifications; the assumptions of each model in Spudich et al., (2014) had a stronger effect on the predictions than did the data. As a result, this study focuses on strike-slip earthquakes. A future update will address directivity effects for other styles of faulting. A future update may also address directionality by providing models for the fault-normal and fault-parallel orientations (e.g., Somerville et al., 1997).

Declaration of conflicting interests

The author(s) declared no potential conflicts of interest with respect to the research, authorship, and/or publication of this article.

ORCID iD

Jeff Bayless (iD) https://orcid.org/0000-0003-1754-2028

Data and Resources

The Pacific Earthquake Engineering Research Center ground-motion database is available at https://ngawest2.berkeley.edu/. The open-source PSHA code HAZ is available at https://github.com/abrahamson/HAZ. Figures shown in this paper were created using MATLAB version: 9.14.0 (R2023a; The MathWorks Inc., 2024). All simulations used to develop the directivity model are available from Bayless et al. (2020) at https://earthquake.usgs.gov/cfusion/external_grants/reports/G18AP00092.pdf. Supplemental Appendix A provides model implementations in MATLAB and FORTRAN. The supplemental material includes additional notes and analyses on directivity centering, calculation of the directivity model parameters, an outline of the model development and example applications. All websites were last accessed July 2024.

Supplemental material

Supplemental material for this article is available online.

References

Aagaard B, Hall JF and Heaton TH (2004) Effects of Fault Dip and Slip Rake Angles on Near-Source Ground Motions: Why Rupture Directivity was Minimal in the 1999 Chi-Chi, Taiwan Earthquake, *Bull. Seismol. Soc. Am.*, 94: 155–170.

Abrahamson NA, Somerville P and Cornell CA (1990) Uncertainty in Numerical Strong Motion Predictions. *Proceedings, Fourth U.S. National Conference Earthquake Engineering*, Palm Springs, CA, May 20-24, 1990, Vol. I, pp. 407–416.

Abrahamson NA (2000) Effects of rupture directivity on probabilistic seismic hazard analysis, *Proceedings from the 6th International Conference on Seismic Zonation*, Palm Springs, California.

Abrahamson NA, Silva WJ and Kamai R (2014) Summary of the ASK14 Ground Motion Relation for Active Crustal Regions. *Earthquake Spectra: August 2014*, Vol. 30, No. 3, pp. 1025–1055.

Abrahamson NA (2024) HAZ, Github Repository, https://github.com/abrahamson/HAZ

Aki KT and Richards P (1980) *Quantitative Seismology*. New York: Freeman.

Al Atik L, Gregor N, Mazzoni S, et al. (2023) Directivity-based probabilistic seismic hazard analysis for the state of California: Report 2, directivity implementation, The B. *John Garrick Institute for the Risk Sciences, Technical Report GIRS-2023-05*, doi: 10.34948/N3KS3B

AlAtik L, Abrahamson NA, Cotton F and et. al. (2010). The variability of ground-motion prediction models and its components. *Seismological Research Letters;* 81(5):794–801.

Ancheta TD, Darragh RB, Stewart JP, et al. (2014). NGA-West2 database. *Earthquake Spectra*. 30. 10.1193/070913EQS197M.

Baker J, Bradley B and Stafford P (2021) *Seismic Hazard and Risk Analysis*. Cambridge University Press; https://doi.org/10.1017/9781108425056

Bayless J and Abrahamson NA (2023) Informing Rupture Directivity Modeling with CyberShake Simulations. Final Report. SCEC Award #22056

Bayless J and Somerville P (2013). Bayless-Somerville Directivity Model, Chapter 3 of PEER Report No. 2013/09, P. Spudich (Editor), Pacific Earthquake Engineering Research Center, Berkeley, CA.

Bayless J, Somerville P and Skarlatoudis A (2020) A Rupture Directivity Adjustment Model Applicable to the NGA-West2 Ground Motion Models and Complex Fault Geometries. Final report. USGS Award No. G18AP00092.

Ben-Zion Y and Sammis CG (2003) Characterization of fault zones, *Pure Appl. Geophys.* 160, 677–715, doi: 10.1007/PL00012554

Boore DM (2010) Orientation-independent, non-geometric-mean measures of seismic intensity from two horizontal components of motion, *Bull. Seismol. Soc. Am.* 100, 1830–1835.

Boore DM, Stewart JP, Seyhan E, et al. (2014) NGA-West2 Equations for Predicting PGA, PGV, and 5% Damped PSA for Shallow Crustal Earthquakes. *Earthquake Spectra* 30:3, 1057–1085.

Campbell KW and Bozorgnia Y (2014) NGA-West2 Ground Motion Model for the Average Horizontal Components of PGA, PGV, and 5% Damped Linear Acceleration Response Spectra. *Earthquake Spectra* 30:3, 1087–1115.

Chiou B, Darragh R, Gregor N, et al. (2008) NGA Project Strong-Motion Database. *Earthquake Spectra;* 24(1):23–44. doi:10.1193/1.2894831

Chiou BSJ and Spudich P (2013) The Chiou and Spudich Directivity Predictor DPP, in Chapter 6 of PEER Report No. 2013/09, P. Spudich (Editor), Pacific Earthquake Engineering Research Center, Berkeley, CA.

Chiou BSJ and Youngs RR (2014) Update of the Chiou and Youngs NGA model for the average horizontal component of peak ground motion and response spectra, *Earthquake Spectra* 30, 1117–1153.

Colavitti L, Lanzano G, Sgobba S, et al. (2022). Empirical evidence of frequency-dependent directivity effects from small-to-moderate normal fault earthquakes in Central Italy. *Journal of Geophysical Research: Solid Earth*, 127, e2021JB023498. https://doi.org/10.1029/2021JB023498

Donahue JL, Stewart JP, Gregor N, et al. (2019) Ground-Motion Directivity Modeling for Seismic Hazard Applications. PEER Report 2019/03

Field EH, Biasi GP, Bird P, et al. (2013) Uniform California earthquake rupture forecast, version 3 (UCERF3)—The time-independent model: U.S. Geological Survey Open-File Report 2013–1165, 97 p., California Geological Survey Special Report 228, and Southern California Earthquake Center Publication 1792, http://pubs.usgs.gov/of/2013/1165/.

Graves RW and Pitarka A. (2014). Refinements to the Graves and Pitarka (2010) Broadband Ground-Motion Simulation Method. *Seis. Res. Letters*. Dec 17, 2014, 12:26. doi: 10.1785/0220140101

Gregor N, Abrahamson NA, Atkinson GM, et al. (2014) Comparison of NGA-West2 GMPEs. *Earthquake Spectra*. 30(3):1179–1197

Hale C, Abrahamson NA and Bozorgnia Y (2018). Probabilistic Seismic Hazard Analysis Code Verification, PEER Report No. 2018/03, 139pp.

Kelly B, Withers KB and Moschetti MP (2022). Development of a seismic directivity adjustment model to the median and aleatory variability of ground motion models, AGU Fall Meeting Abstracts, 12–16 December 2022, Chicago, Illinois, U.S.A., 2022AGUFM.S46A.01K

Liou IY and Abrahamson NA (2024) Aleatory Variability and Epistemic Uncertainty for Ground-Motion Models in PSHA, Submitted to Bulletin of the Seismological Society of America.

Melgar D and Hayes G (2019). The Correlation Lengths and Hypocentral Positions of Great Earthquakes. *Bulletin of the Seismological Society of America*. 109(6):2582–2593

Meng X, Goulet CA, Milner K, et al. (2023) Comparison of Nonergodic Ground-Motion Components from CyberShake and NGA-West2 Datasets in California, *Bull. Seismol. Soc. Am.* 113(3): 1152–1175. doi: 10.1785/0120220049

Petersen MD, Shumway AM, Powers PM, et al. (2024) The 2023 US 50-State National Seismic Hazard Model: Overview and implications. *Earthquake Spectra*. 40(1):5–88. doi:10.1177/87552930231215428

Rodriguez-Marek A and Cofer W (2009) Incorporation to Forward-Directivity into Seismic Hazard Analysis. Report prepared for Transportation Northwest. Report No. TNW2009-02, Research Agreement No. 430846

Rowshandel B (2013) Rowshandel's NGA-West2 directivity model, Chapter 3 of PEER Report No. 2013/09, P. Spudich (Editor), Pacific Earthquake Engineering Research Center, Berkeley, CA.

Rowshandel B (2018) Directivity Centering of GMPEs and Directivity Models. *Eleventh US National Conference on Earthquake Engineering*, June 25-29, 2018, Los Angeles, California.

Somerville PG, Smith N, Graves RW, et al. (1997) Modification of empirical strong ground motion attenuation relations for the amplitude and duration effects of rupture directivity. *Seismol. Res. Lett.* 68, 199–222.

Somerville PG (2003) Magnitude scaling of the near fault rupture directivity pulse. *Physics of the Earth and Planetary Interiors* 137, 201–212.

Spudich P and Chiou BSJ (2013) The Spudich and Chiou NGA-West2 directivity model, Chapter 5 of PEER Report No. 2013/09, P. Spudich (Editor), Pacific Earthquake Engineering Research Center, Berkeley, CA.

Spudich P and Chiou BSJ (2015) Strike-Parallel and Strike-Normal Coordinate System Around Geometrically Complicated Rupture Traces- Use by NGA-West2 and Further Improvements. US Geological Survey Open File Report 2015-1028, 28p.

Spudich P, Bayless J, Baker JW, et al. (2013) Final Report of the NGA-West2 Directivity Working Group, Pacific Earthquake Engineering Research Center Report PEER-2013/09, Berkeley, CA, 130 pp.

Spudich P, Rowshandel B, Shahi SK, et al. (2014). Comparison of NGA-West2 Directivity Models. *Earthquake Spectra Aug* 2014, Vol. 30, No. 3 pp. 1199–1221

The MathWorks Inc. (2024). MATLAB version: 9.14.0 (R2023a), Natick, Massachusetts: The MathWorks Inc. https://www.mathworks.com

Watson-Lamprey JA (2018) Capturing directivity effects in the mean and aleatory variability of the NGA-West 2 ground motion prediction equations, PEER Report No. 2018/04, Pacific Earthquake Engineering Research Center, University of California, Berkeley, CA.

Weatherill G and Lilienkamp H (2023). Capturing Directivity in Probabilistic Seismic Hazard Analysis for New Zealand: Challenges, Implications, and a Machine Learning Approach for Implementation. *Bulletin of the Seismological Society of America*; doi: https://doi.org/10.1785/0120230161

Withers K, Moschetti M, Powers P, et al. (2024) Integration of Seismic Directivity Models for the US National Seismic Hazard Model. *Earthquake Spectra*. 2024;40(2):1066–1098. doi:10.1177/87552930241232708